The Journal of Chemical Physics

Peltier effects in lithium-ion battery modeling

Cite as: J. Chem. Phys. **154**, 114705 (2021); https://doi.org/10.1063/5.0038168
Submitted: 19 November 2020 . Accepted: 22 February 2021 . Published Online: 15 March 2021

Lena Spitthoff, Astrid Fagertun Gunnarshaug, Dick Bedeaux, Odne Burheim, and Signe Kjelstrup

The Journal of Chemical Physics ARTICLE scitation.org/journal/jcp

Peltier effects in lithium-ion battery modeling

Cite as: J. Chem. Phys. 154, 114705 (2021); doi: 10.1063/5.0038168
Submitted: 19 November 2020 • Accepted: 22 February 2021 •
Published Online: 15 March 2021

Lena Spitthoff,[1] Astrid Fagertun Gunnarshaug,[2] Dick Bedeaux,[2] Odne Burheim,[1] and Signe Kjelstrup[2,a)]

AFFILIATIONS

[1] Department of Energy and Process Engineering, Norwegian University of Science and Technology, NO-7491 Trondheim, Norway

[2] PoreLab, Department of Chemistry, Norwegian University of Science and Technology, NO-7491 Trondheim, Norway

Note: This paper is part of the JCP Special Collection in Honor of Women in Chemical Physics and Physical Chemistry.
[a)] **Author to whom correspondence should be addressed:** signe.kjelstrup@ntnu.no

ABSTRACT

A high battery temperature has been shown to be critical for lithium-ion batteries in terms of performance, degradation, and safety. Therefore, a precise knowledge of heat sources and sinks in the battery is essential. We have developed a thermal model for lithium-ion batteries, a model that includes terms not included before, namely, Peltier and Dufour heat effects. The model is derived using non-equilibrium thermodynamics for heterogeneous systems, the only theory which is able to describe in a systematic manner the coupling of heat, mass, and charge transport. The idea of this theory is to deal with surfaces as two-dimensional layers. All electrochemical processes in these layers are defined using excess variables, implying, for instance, that the surface has its own temperature. We show how the Peltier and Dufour heats affect a single cell and may produce an internal temperature rise of 8.5 K in a battery stack with 80 modules. The heat fluxes leaving the cell are also functions of these reversible heat effects. Most of the energy that is dissipated as heat occurs in the electrode surfaces and the electrolyte-filled separator. The analysis shows that better knowledge of experimental data on surface resistances, transport coefficients, and Dufour and Peltier heats is essential for further progress in thermal modeling of this important class of systems.

I. INTRODUCTION

The transition from fossil fuels to renewable power sources requires reliable energy storage technologies. Lithium-ion batteries (LIBs) have become the leading energy storage technology in many sectors due to superior properties, such as high gravimetric and volumetric energy densities, high efficiency, and compatibility with the existing electric infrastructure.[1] New demands from the transport sector (e.g., electric ferries, planes, and cars) have now an increasing impact on the LIB market. Those applications require large battery packs, high energy and power density, and possibilities for large charging and discharging rates. Issues with safety, aging of cells, and loss of capacity are then important. These issues, in particular, have been shown to be temperature dependent.[2–7] It is well known[7,8] that good thermal management is essential for safety, performance, and life-time expectancy in lithium-ion batteries. The demand for faster charging or discharging and reliability of large battery-pack operations call for good thermal management and, in turn, a very accurate thermal model.

Several types of heat effects can be observed when electric current is drawn from an electrochemical cell.[9] There is irreversible heat generation due to electric resistances (i.e., Joule heating) and due to electrode overpotentials (resistances to the electrochemical reactions).[10] Joule heat is associated with the paths of the charge carrier (the ion transport in the electrolyte and the electron transport in the solid-state materials and metals). In addition, there is heat released or absorbed reversibly at the electrode interfaces.[11] In batteries, the reversible heat effects are entropic, and in LIB, they are due to intercalation/de-intercalation reactions at the electrode–electrolyte interface. The overall reversible heat effect is given by the entropy of the cell reaction.[10,11] Locally, at each electrode surface, the reversible heat effect is the so-called Peltier heat.[11,12] In addition, the Dufour effect adds a reversible term to the expression for the heat flux or to the Peltier heat, e.g., the heat of transfer times the molar flux of all moving components[12] [see Eqs. (10) and (11)].

The heat released or absorbed in a unit cell will thus not be uniformly distributed over the cell. The electrodes and electrolyte have different resistances, leading to a varying Joule heating across

the cell. The overpotentials differ between the two electrode surfaces. The reversible Peltier and Dufour effects may even lead to cooling, depending on the direction of the electric current. If an electrode Peltier effect leads to heating during the discharging process, it will lead to cooling while charging.[11] All together, this leads to development of temperature gradients, and of a thermal driving force, which again affects transport of mass and creates concentration gradients within the electrolyte. Neither the Peltier heat nor the Dufour effect is usually included in battery modeling. They have been discussed by several authors, however.[9,13–16]

It is the purpose of this work to give a full account of Peltier heat effects in a single battery model and in stacks up to 80 single cells. Our battery model will be simple in one respect; we consider mostly a uniform electrolyte. However, we also compute how the battery approaches a stationary state temperature profile in the presence of conditions when there is a balance of thermal and chemical forces in the electrolyte. This means that Dufour effects will be computed, but only for stationary state battery operation. The impact of time-dependent diffusion of electrolyte components on the temperature profile development will be examined later.

A common misunderstanding seen in the literature[17] is that the Peltier heat of an electrode can be determined from the temperature variation of the electromotive force, *emf*, using lithium as a counter electrode. This variation leads, however, to the cell reaction entropy times the temperature of the cell and not to the Peltier heat of the single electrode. This misunderstanding is often made citing Newman,[18] despite Newman's statement that the entropy change is related to the sum of reversible heat effects for the whole cell at isothermal conditions[19] [see Eq. (92) in the supplementary material]. Rao and Newman mentioned the Peltier heat at the electrode surface in a model for the heat generation rate in insertion battery systems but did not include this effect in their simulation due to a lack of data.[10] We are in a similar situation with respect to the Dufour effect. As far as we know, there are no experimental reports available on the heat of transfer or Soret coefficient of battery electrolytes. This currently limits our exploration of the Dufour effect.

The electrode–electrolyte interface is essential for the battery function, in particular, away from the open circuit potential, the *emf*. Irreversible growth of the solid electrolyte interphase (SEI)[2,20] that enhances battery degradation has been observed. The lack of stability, which occurs at high temperatures, has been associated with degradation or loss of lithium-ions.[20,21] The SEI resistivity is therefore probably larger than that of the near surroundings. At low temperatures and high charging rates, lithium plating becomes an issue at the anode surface.[5]

The transports of heat, mass, and charge in LIB are highly coupled, meaning that one type of transport does not occur without the others. The theory to describe such coupling is non-equilibrium thermodynamics. This theory was recently developed to deal with heterogeneous systems, where bulk phases as well as surfaces are present and play important roles,[12] precisely what is the case in LIB. The battery consists of a cathode and an anode separated by an electrolyte-soaked separator (see Fig. 1 for a schematic illustration of the three bulk phases). The bulk of the cathode and anode of the LIB are usually made of grains of various intercalating compounds. They are nanoporous (including lithium-ions) and microporous (with electrolyte-filled pores). The electrolyte is usually a mix

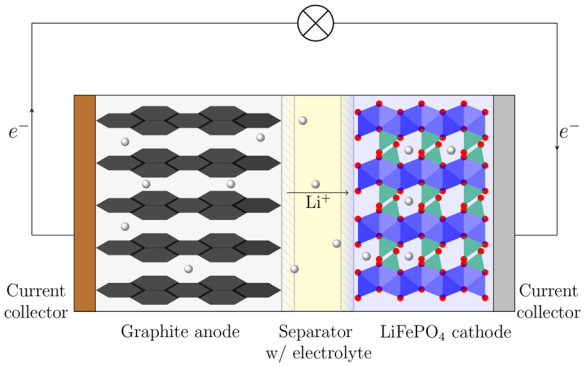

FIG. 1. Schematic illustration of a LIB (during discharge) with a graphite anode C_6 (left) and a lithium iron phosphate cathode $LiFePO_4$ (right). The electrolyte contains a lithium salt and conducts by Li^+. The region where the reaction takes place is the electrode surface, sandwiched between electrode–electrolyte boundaries.

of several organic carbonates, such as ethylene carbonate and diethyl carbonate, and a lithium salt, most often $LiPF_6$.[2]

The electrode reactions are happening at the interface of active material grains with the electrolyte. The left-hand side of Fig. 2 provides a schematic illustration of those active electrode material grains. In the real application, the electrode–electrolyte interfaces are distributed throughout the whole electrode bulk material, as it consists of single particles and is soaked with electrolyte. In our model, we simplify this situation and consider three bulk phases, the anode, the separator, and the cathode, separated by sharp interfaces left and right: the anode and cathode surface. This simplification is schematically shown on the right-hand side of Fig. 2. We will discuss the consequences of this simplification in the later.

We shall apply non-equilibrium thermodynamics theory to LIB using the special way to deal with heterogeneous layers introduced by Bedeaux *et al.*[22] The method was recently used successfully by Sauermoser *et al.* to describe polymer electrolyte fuel cells.[23] The surfaces are then defined using Gibbs excess variables (cf. Refs. 12, 23, and 24). The surfaces are therefore 2D-systems and are represented by thin vertical lines in Fig. 1. We chose the fluxes of the neutral components as independent fluxes. The entropy production is independent of the choice. The electric current density, as defined in the external circuit, is used to measure net charge transport.[12] In such a formulation of the surface, it will, e.g., have its own temperature. Local variables are given per unit of surface area.

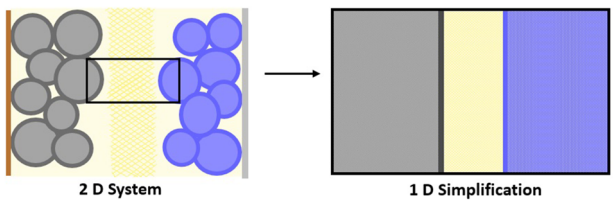

FIG. 2. Schematic illustration of the system. On the left is shown the porous structure of the electrodes, consisting of grains surrounded by the electrolyte. To the right is shown the simplified system that is modeled.

We shall present and solve numerically a 1D model of the LIB using the principles of non-equilibrium thermodynamics. The full derivation, including all intermediate steps, is available in supplementary material. The essential equations are extracted below. By this division of the theoretical part of the work, we hope to bring forward the physics of the battery model in a clearer way.

We first present the equations needed to solve the electric potential profile and the accompanying temperature profile through the battery for cases when lithium-ion transports all charge and no diffusion takes place. We next solve the set of equations and determine the time-evolution of a single battery potential profile and temperature profile to the stationary state. We report results also for a battery stack of 4, 20, and 80 single cells. The heat fluxes out of the battery will be determined, and the local dissipation of energy will be found. A sensitivity analysis will be done to study the importance of the interface properties, in particular, the interface resistances. Under isothermal conditions and uniform composition of the electrolyte, the equations reduce to those usually found in the literature.

We aim to make clear that the coupling terms and the surface properties of the model are essential for the understanding of the battery thermal signature. They all make significant contributions to a time-dependent battery and stack temperature profile.

II. THE THERMODYNAMIC SYSTEM

For modeling purposes, we simplify the part of the battery that contains the electrode reactions. This part is made from grains that were wetted with electrolyte components. Every particle has an interface with the electrolyte phase. It is also in contact with the current collector. We shall use the words interface and surface interchangeably to mean the layer between the electrolyte and the active solid electrode, where the electrode reaction takes place. In reality, this layer is not infinitely thin; its finite thickness is δ. Figure 2 illustrates schematically the 2 D system on the left and the 1 D simplified model on the right. The interface region between the electrode grains and the electrolyte is simplified as a sharp surface in the model.

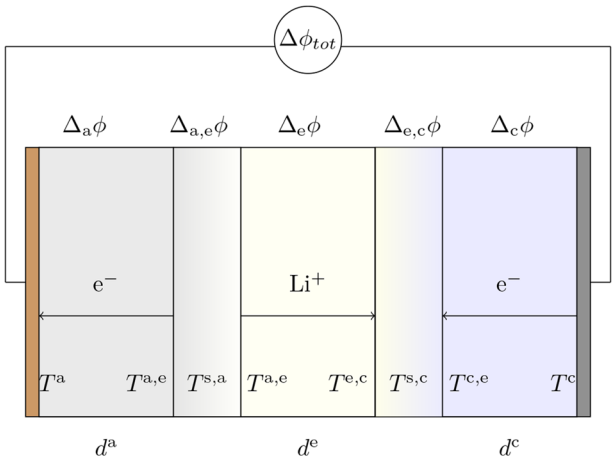

FIG. 3. The notation used to describe the five layers of a LIB. Lithium-ion is the sole charge carrier in the electrolyte, the central layer. The anode bulk is pictured on the left-hand side, while the cathode bulk is pictured on the right-hand side, both with electrons as conductors. The thin interface layers contain the region where the electrode reactions take place, the anode reaction in the second layer and the cathode reaction in the fourth layer. The first superscript refers to the phase we are in: a for the anode, e for the electrolyte, and c for the cathode. The second superscript refers to the adjacent phase. The subscript(s) on the symbol Δ refer to the anode or cathode thickness, a or c, or to the jump across an interface, say, from a to e.

We consider three homogeneous (bulk) phases separated by two interfaces or surfaces. The thermodynamic system is further illustrated in Fig. 3. The cell has five layers, and an outer circuit. There is a potential and temperature drop across each layer that we shall compute. Figure 3 explains the notation used: a for the bulk anode, c for the bulk cathode, and e for the electrolyte. The subscript of the difference symbol Δ indicates the layer it applies to (a, e, or c). The interface regions are a, e (or e, c) meaning from a to e (or e to c). The first superscript indicates the phase or surface, while the second superscript is the adjacent phase. For more details on terminology and a symbol list, see the supplementary material and a textbook[12] on the theory.

III. MODEL

In this work, we consider transport normal to the interfaces only, averaging thus over a cross-sectional area of 1 m^2. We do not know the real contact area between the electrode and the electrolyte (see Fig. 2), so we refer all fluxes and surface coefficients to the cross-sectional area of the cell. The surface of the model is infinitely thin. The systematic approach is as follows: We give the entropy production for each bulk layer and the constitutive equations that follow from this. In the next round, we give the corresponding equations for the interfaces. For each layer, we present equations for the electric potential drop and the equations that give the corresponding variation in the temperature.

A. Entropy production and flux equations for the bulk layers

The entropy production, σ, of a control volume in one of the bulk phases can be generally written as

$$\sigma = J'_q \frac{\partial}{\partial x}\left(\frac{1}{T}\right) - \sum_{i=1}^{n-1} J_i \frac{1}{T}\left(\frac{\partial \mu_{i,T}}{\partial x}\right) - j\frac{1}{T}\left(\frac{\partial \phi}{\partial x}\right), \tag{1}$$

where J'_q is the measurable heat flux with the subscript q referring to heat, $\partial/\partial x$ is the partial derivative in the x-direction, T is the temperature, J_i and $\mu_{i,T}$ is the flux and chemical potential at constant temperature of component i, respectively, j is the current density, and ϕ is the electric potential. The supplementary material provides a complete derivation of the equations that follow. We extract the particular set of equations that are needed for the numerical solution.

The entropy production defines the force-flux or the constitutive relations of the three bulk phases,

$$J'_q = -\lambda\frac{\partial T}{\partial x} + \sum_{i=1}^{n-1} q_i^*\left(J_i - \frac{t_i}{F}j\right) + \frac{\pi}{F}j, \tag{2}$$

$$J_i = -c_i D_{i,T}\frac{\partial T}{\partial x} - \sum_{k=1}^{n-1} D_{ik}\frac{\partial c_k}{\partial x} + \frac{t_i}{F}j, \tag{3}$$

$$\left(\frac{\partial \phi}{\partial x}\right) = -\frac{\pi}{FT}\frac{\partial T}{\partial x} - \sum_{i=1}^{n-1}\frac{t_i}{F}\left(\sum_{k=1}^{n-1} a_{ik}\frac{\partial \ln c_k}{\partial x}\right) - rj, \tag{4}$$

where λ is the stationary state, through-plane thermal conductivity, q_i^* and t_i are the heat of transfer and the transference coefficient of component i, respectively, F is Faraday's constant, π is the Peltier coefficient, c_i and $D_{i,T}$ are the concentration and thermal diffusion coefficient of component i, D_{ik} is the interdiffusion coefficient of i and k, a_{ik} is a coefficient relating the chemical potential gradient to the logarithm of the concentration gradient, and r is the ohmic resistivity. The heat of transfer, which is a measure of the Dufour effect, is defined as $q_i^* = (J_q'/J_i)_{j=0,dT=0,J_{k\neq i}=0}$, the transference coefficient is defined as $t_i = (J_iF/j)_{dT=0,dc_i=0}$, while the Peltier coefficient is defined as $\pi^i = (J_q'F/j)_{dT=0,dc_i=0}$. We refer to the supplementary material for a complete derivation and more details. A flux is positive, when the direction of transport is from the left to the right.

1. Electrode bulk phase

In the electrode, all of the electric current is carried by electrons, with lithium chosen as the frame of reference. The flux of electrons is then equal to the current density, $J_{e^-} = -j/F$. The velocity of electrons within the electrode will be much higher than any velocity of the host structure, Θ, so the flux of electrons will be much larger than any velocity of the host structure, i.e., $J_\Theta = c_\Theta v_\Theta \ll j/F$, where v_Θ is the velocity of the host structure. We can therefore assume that $t_\Theta \approx 0$. The concentration of Li in graphite is denoted c_θ. When this is the only variable concentration, all terms containing summation signs disappear from Eqs. (2)–(4). This simplifies the flux-force Eqs. (2)–(4) for the electrode to

$$J_q' = -\lambda\frac{\partial T}{\partial x} + q_\Theta^* J_\Theta + \frac{\pi}{F}j, \tag{5}$$

$$J_\Theta = -c_\Theta D_{\Theta,T}\frac{\partial T}{\partial x} - D_\Theta\frac{\partial c_\Theta}{\partial x}, \tag{6}$$

$$\frac{\partial \phi}{\partial x} = -\frac{\pi}{FT}\frac{\partial T}{\partial x} - rj. \tag{7}$$

From the definition of the Peltier coefficient (see the supplementary material),[12] we have for the anode and the cathode phases

$$\begin{aligned}\pi^{\mathrm{a}}(x) &= -TS_{e^-}^{*,\mathrm{a}},\\ \pi^{\mathrm{c}}(x) &= -TS_{e^-}^{*,\mathrm{c}}.\end{aligned} \tag{8}$$

The Peltier coefficients of the electrodes consist of the heat transported with the charge carrier, here the product $TS_{e^-}^{*,\mathrm{a}}$. The entropy transported, $S_{e^-}^*$, through the electrode to the interface is that of the electrons. By integrating across the thickness of the electrode, the contributions to the electric potential become

$$\begin{aligned}\Delta_{\mathrm{a}}\phi &= \frac{S_{e^-}^{*,\mathrm{a}}}{F}\Delta_{\mathrm{a}}T - r^{\mathrm{a}}jd^{\mathrm{a}},\\ \Delta_{\mathrm{c}}\phi &= \frac{S_{e^-}^{*,\mathrm{c}}}{F}\Delta_{\mathrm{c}}T - r^{\mathrm{c}}jd^{\mathrm{c}},\end{aligned} \tag{9}$$

where d^{a} and d^{c} are the thicknesses of the anode and cathode bulk phase, respectively (see Fig. 3).

2. Electrolyte bulk phase

The salt and the solvent molecules of the electrolyte are contained in a separator material. We assume that due to large pore-sizes, the separator is inert. It will then not appear in the entropy production. The flux-force equations will be those presented above [cf. Eqs. (2)–(4)]. We choose the anions of the lithium salt (here $LiPF_6$) as a frame of reference. The current is then only carried by lithium-ions in the electrolyte and not by anions. In the electrolyte, the entropy transported with Li^+ is $S_{Li^+}^*$. From the definition of the Peltier coefficient of the electrolyte, we have[25]

$$\pi^{\mathrm{e}} = TS_{Li^+}^* + \sum_{i=1}^{n-1} t_i q_i^*. \tag{10}$$

The Peltier coefficient contains the transported entropy of lithium-ion and, in addition, the heat q_i^* that is carried electro-osmotically with neutral components i. This is expressed by the product of the transference coefficient with q_i^* (see the supplementary material for more details). We expect this effect to be significant only for the electrolyte. Neither the heats of transfer, q_i^*, nor the transported entropy is a small quantity.[24]

By integrating across the thickness of the electrolyte, d^{e}, with constant transport properties, we find the contribution from the electrolyte to the electric potential,

$$\begin{aligned}\Delta_{\mathrm{e}}\phi = &-\frac{S_{Li^+}^{*,\mathrm{e}}}{F}\Delta_{\mathrm{e}}T - \sum_{i=1}^{n-1}\frac{t_i q_i^{*,\mathrm{e}}}{F}\Delta_{\mathrm{e}}\ln T\\ &- \sum_{i,k=1}^{n-1}\frac{t_i^{\mathrm{e}}}{F}a_{ik}\Delta_{\mathrm{e}}\ln c_k - r^{\mathrm{e}}jd^{\mathrm{e}}.\end{aligned} \tag{11}$$

We see here how the transported entropy and the heat of transfer contribute to the electric potential difference across the phase.

B. The electrode surfaces

The electrochemical reaction at the anode surface (during discharge) is

$$\mathrm{Li} - \Theta \rightarrow \mathrm{Li}^+ + \mathrm{e}^- + \Theta.$$

The following identity holds:

$$J_{\mathrm{Li}} = j/F. \tag{12}$$

That is, the flux of neutral lithium into the surface from the left-hand side must always be equal to the flux of charged species out of the surface into the electrolyte. We start in the host structure frame of reference, so $J_\Theta^{\mathrm{a}} = 0$ (see the supplementary material). With dependency (12), the entropy production for the anode surface during discharge is given by

$$\begin{aligned}\sigma^{\mathrm{s,a}} = &J_q'^{\mathrm{a,e}}\left(\Delta_{\mathrm{a,s}}\frac{1}{T}\right) + J_q'^{\mathrm{e,a}}\left(\Delta_{\mathrm{s,e}}\frac{1}{T}\right)\\ &- \sum_{k=1}^{n} J_k^{\mathrm{e,a}}\frac{\Delta_{\mathrm{s,e}}\mu_{k,T}(T^{\mathrm{s,a}})}{T^{\mathrm{s,a}}} - j\left(\frac{\Delta_{\mathrm{a,e}}\phi}{T^{\mathrm{s,a}}}\right) - \frac{j}{F}\frac{\Delta_n G^{\mathrm{s,a}}}{T^{\mathrm{s,a}}}\end{aligned} \tag{13}$$

(see Fig. 3 and the supplementary material for notation). The electric potential difference, $\Delta_{\mathrm{i,o}}\phi = \phi^{\mathrm{o,i}} - \phi^{\mathrm{i,o}}$, is due to the reaction Gibbs energy by conversion of neutral components,[12] $\Delta_n G^{\mathrm{s}}$. The flux-force equations for the anode surface become

$$J_q'^{\mathrm{a,e}} = -\lambda_{\mathrm{a}}^{\mathrm{s,a}}\Delta_{\mathrm{a,s}}T + \frac{\pi^{\mathrm{a}}}{F}j, \tag{14}$$

$$J_q'^{\mathrm{e,a}} = -\lambda_{\mathrm{e}}^{\mathrm{s,a}}\Delta_{\mathrm{s,e}}T + \sum_{k=1}^{n-1} q_k^{*,\mathrm{e}}\left(J_k^{\mathrm{e,a}} - \frac{t_k^{\mathrm{e}}}{F}j\right) + \frac{\pi^{\mathrm{e}}}{F}j, \tag{15}$$

$$J_i^{\mathrm{e,a}} = -\sum_{k=1}^{n-1}\frac{L_{ik}^{\mathrm{s}}}{T^{\mathrm{s}}}\Delta_{\mathrm{s,e}}\mu_{k,T} - c_i^{\mathrm{s}}D_{i,T}\Delta_{\mathrm{s,e}}T + \frac{t_i^{\mathrm{e}}}{F}j, \tag{16}$$

$$-\left(\Delta_{\mathrm{a,e}}\phi + \frac{\Delta_n G^{\mathrm{s}}}{F}\right) = \frac{\pi^{\mathrm{a}}}{FT^{\mathrm{a}}}\Delta_{\mathrm{a,s}}T + \frac{\pi^{\mathrm{e}}}{FT^{\mathrm{e}}}\Delta_{\mathrm{s,e}}T + \sum_{i=1}^{n-1}\frac{t_i}{F}\Delta_{\mathrm{s,e}}\mu_{i,T} + r^{\mathrm{s,a}}j. \tag{17}$$

We see for *emf* conditions ($j = 0$) and constant temperature that the Nernst equation is recovered from the last parentheses in Eq. (17) (see Ref. 12, Chap. 10 for more details on the relation to the Maxwell potential). For the anode,

$$\frac{\Delta_n G^{\mathrm{s,a}}}{F} = -\frac{1}{F}\mu_{\mathrm{Li_x-\Theta}}^{\mathrm{s,a}}, \tag{18}$$

and for the cathode,

$$\frac{\Delta_n G^{\mathrm{s,c}}}{F} = \frac{1}{F}\mu_{\mathrm{Li_x-\Theta}}^{\mathrm{s,c}}, \tag{19}$$

where $\mu_{\mathrm{Li_x-\Theta}}$ is the chemical potential of Li − Θ at the electrode surface for the lithiated state expressed by x. This will for simplicity be written as $\mu_{\mathrm{Li(x)}}$.

The full contribution to the cell potential from the anode is now given by

$$\Delta_{\mathrm{a,e}}\phi = \frac{1}{F}\mu_{\mathrm{Li(x)}}^{\mathrm{s,a}} - \frac{\pi^{\mathrm{a}}}{FT^{\mathrm{a}}}\Delta_{\mathrm{a,s}}T - \frac{\pi^{\mathrm{e}}}{FT^{\mathrm{e}}}\Delta_{\mathrm{s,e}}T - \sum_{i=1}^{n-1}\frac{t_i^{\mathrm{e}}}{F}\Delta_{\mathrm{s,e}}\mu_{i,T} - r^{\mathrm{s,a}}j, \tag{20}$$

where Eq. (10) was introduced in the last equality. An equivalent derivation for the cathode surface gives

$$\Delta_{\mathrm{e,c}}\phi = -\frac{1}{F}\mu_{\mathrm{Li(x)}}^{\mathrm{s,c}} - \frac{\pi^{\mathrm{e}}}{FT^{\mathrm{e}}}\Delta_{\mathrm{s,e}}T - \frac{\pi^{\mathrm{c}}}{FT^{\mathrm{c}}}\Delta_{\mathrm{s,c}}T - \sum_{i=1}^{n-1}\frac{t_i^{\mathrm{e}}}{F}\Delta_{\mathrm{e,s}}\mu_{i,T} - r^{\mathrm{s,c}}j. \tag{21}$$

We are now in position to find the total cell potential.

C. The cell potential profile

We can now compute at any time the electric potential profile through the cell in terms of differences across the bulk phases and jumps at each interface using Eqs. (9), (11), (20), and (21) (see the supplementary material). The sum of all contributions is

$$\Delta\phi_{\mathrm{tot}} = \Delta_{\mathrm{a}}\phi + \Delta_{\mathrm{a,e}}\phi + \Delta_{\mathrm{e}}\phi + \Delta_{\mathrm{e,c}}\phi + \Delta_{\mathrm{c}}\phi. \tag{22}$$

The time-variation in the electric potential can come from heat accumulation and concentration gradients created in the electrolyte [see Eq. (11)], plus from changes in the reaction Gibbs energy[26,27] in the electrodes with the changing state of charge (SOC) [see Eqs. (20) and (21)]. We consider the first as superimposed on the second stationary state in this work.

At isothermal conditions and uniform electrolyte, this reduces to

$$\Delta\phi_{\mathrm{tot}} = -\frac{1}{F}\Delta\mu_{\mathrm{Li(x)}} - r^{\mathrm{a}}jd^{\mathrm{a}} - r^{\mathrm{s,a}}j - r^{\mathrm{e}}jd^{\mathrm{e}} - r^{\mathrm{s,c}}j - r^{\mathrm{c}}jd^{\mathrm{c}}. \tag{23}$$

The main contribution to the battery potential loss comes from the surface potential drops. The open circuit voltage of a LFP/graphite battery is about 3.4 V at 100% SOC.[28,29] This is the maximum voltage during discharge when there are no resistance losses. The losses shown here are ohmic losses in the bulk phases and in the electrode surfaces. The overpotential at each electrode, $\eta^{\mathrm{s,i}}$, with i = a or c, will be interpreted as the resistance to the electrochemical reaction in the surface. This gives

$$\eta^{s} = r^{\mathrm{s,i}}j = \frac{2RT}{F}\ln\left(\frac{j}{j_{0,\mathrm{i}}}\right). \tag{24}$$

The last equality is the Tafel equation, where the exchange current density of the intercalation reaction is $j_{0,\mathrm{i}}$.[30,31]

D. The time-variation of the temperature profile

The expression for the time-variation in the temperature is given from the energy balance. For a local volume element in a bulk phase, this is

$$\frac{\partial T}{\partial t} = \frac{1}{\rho C_p}\left[-\frac{\partial}{\partial x}J_q' - \sum_{i=1}^{n} J_i\left(\frac{\partial}{\partial x}H_i\right) - \sum_{i=1}^{n} TS_i\left(\frac{\partial}{\partial x}J_i\right) - \frac{\partial\phi}{\partial x}j\right], \tag{25}$$

where ρ is the density, C_p is the heat capacity, and H_i and S_i the are partial molar enthalpy and partial molar entropy of component i, respectively. The partial molar properties refer to the components in the electrolyte. They add to the measurable heat flux to give the energy flux. The expression was derived in detail in the supplementary material.

For an interface element, we similarly obtain

$$\frac{dT^{\mathrm{s}}}{dt} = \frac{1}{\rho^{\mathrm{s}}C_p}\left[J_q'^{\mathrm{i,o}} - J_q'^{\mathrm{o,i}} - j\left[\phi^{\mathrm{o,i}} - \phi^{\mathrm{i,o}}\right] + \sum_i J_i^{\mathrm{i,o}}H_i^{\mathrm{i,o}} - \sum_j J_j^{\mathrm{o,i}}H_j^{\mathrm{o,i}}\right]. \tag{26}$$

Typical for the interface is the discrete form of the energy balance.

1. Anode and cathode bulk phases

The change in local temperature with time for the anode bulk material is thus [see Eqs. (25) and (5)–(9)]

$$\frac{\partial T^{\mathrm{a}}}{\partial t} = \frac{1}{\rho^{\mathrm{a}}C_p^{\mathrm{a}}}\left[\frac{\partial}{\partial x}\left(\lambda^{\mathrm{a}}\left(\frac{\partial T^{\mathrm{a}}}{\partial x}\right)\right) - J_\Theta^{\mathrm{a}}M_\Theta C_{p,\Theta}^{\mathrm{a}}\frac{\partial T^{\mathrm{a}}}{\partial x} + r^{\mathrm{a}}j^2\right], \tag{27}$$

where M_i is the molar mass of component i. A similar equation is obtained for the cathode bulk material. When we neglect Dufour effects in these bulk phases, we are left with only the first and last terms. These terms represent thermal conductance and ohmic heating of the electrode, respectively.

2. Electrolyte bulk phase

In the same way, we find from Eqs. (25) and (2)–(4) an expression for the temperature change with time in the electrolyte,

$$\frac{\partial T^{\mathrm{e}}}{\partial t} = \frac{1}{\rho^{\mathrm{e}} C_p^{\mathrm{e}}}\left[\frac{\partial}{\partial x}\left(\lambda^{\mathrm{e}}\left(\frac{\partial T^{\mathrm{e}}}{\partial x}\right)\right) - \sum_{i=1}^{n-1} j_i^{\mathrm{e}} M_{\mathrm{i}} C_{p,i}^{\mathrm{e}} \frac{\partial T^{\mathrm{e}}}{\partial x} + \sum_{i=1}^{n-1} \frac{t_i^{\mathrm{e}}}{F} q_i^{*,\mathrm{e}} \frac{\partial \ln T^{\mathrm{e}}}{\partial x} j + \sum_{i=1}^{n-1} \frac{t_i^{\mathrm{e}}}{F}\left(\sum_{l=1}^{n-1} a_{il} \frac{\partial \ln c_l^{\mathrm{e}}}{\partial x}\right) j + r^{\mathrm{e}} j^2\right]. \tag{28}$$

By introducing the stationary state condition, the molar fluxes vanish, and the two terms related to the Dufour effect cancel.[12] We obtain the following expression for the time-variation in the temperature in a control volume of the electrolyte:

$$\frac{\partial T^{\mathrm{e}}}{\partial t} = \frac{1}{\rho^{\mathrm{e}} C_p^{\mathrm{e}}}\left[\frac{\partial}{\partial x}\left(\lambda^{\mathrm{e}}\left(\frac{\partial T^{\mathrm{e}}}{\partial x}\right)\right) + r^{\mathrm{e}} j^2\right]. \tag{29}$$

The first term is the thermal conductance, and the last term represents ohmic heating.

3. The heating or cooling of the electrode surfaces

From Eqs. (26) and (15)–(17), we obtain for the anode surface temperature

$$\frac{\mathrm{d}T^{\mathrm{s,a}}}{\mathrm{d}t} = \frac{1}{\rho^{\mathrm{s,a}} C_p^{\mathrm{s,a}}}\left(-\lambda_{\mathrm{a}}^{\mathrm{s,a}} \Delta_{\mathrm{a,s}} T + \lambda_{\mathrm{e}}^{\mathrm{s,a}} \Delta_{\mathrm{s,e}} T - \frac{\pi^{\mathrm{a,e}}}{F} j + r^{\mathrm{s,a}} j^2 + j \frac{\pi^{\mathrm{a}}}{F T^{\mathrm{a}}} \Delta_{\mathrm{a,s}} T + j \frac{\pi^{\mathrm{e}}}{F T^{\mathrm{e}}} \Delta_{\mathrm{s,e}} T - \sum_{k=1}^{n-1} j \frac{t_k^{\mathrm{e}}}{F} \Delta_{\mathrm{s,e}} \mu_{k,T} + \sum_{k=1}^{n-1} q_k^{*,\mathrm{e}} \frac{t_k^{\mathrm{e}}}{F} j - \sum_{k=1}^{n-1} J_k^{\mathrm{e,a}} \mu_k^{\mathrm{s,e}}\right), \tag{30}$$

where we have defined the Peltier heat (not to be confused with the Peltier coefficient of a bulk phase) of the surface as

$$\pi^{\mathrm{a,e}}(T^{\mathrm{s,a}}) = \pi^{\mathrm{e}} - \pi^{\mathrm{a}} - T^{\mathrm{s,a}} S_{\mathrm{Li(x)}}^{\mathrm{s,a}}. \tag{31}$$

The Peltier heat of an interface arises from an entropy balance at the interface in question. It is the heat that need be delivered to the interface when 1 mol of positive charge is passing in the circuit from left to right.[11] This net heat effect is the sensitive heat that we can measure at the junction during charge transfer. The Peltier heat can be determined from experiments by decomposing phenomena that contribute to Eq. (30). This cumbersome procedure makes the determination inaccurate. Instead, we may measure the reciprocal effect the Seebeck coefficient, and calculate the Peltier heat. We will not go into detail here on this experiment and refer instead to previous work and references therein.[24]

The Peltier heat in Eq. (31) has a contribution from the Dufour effect when the electrolyte is homogeneous [cf. Eq. (10)]. We refer to this expression as the initial Peltier heat, $\pi_{t=0}^{\mathrm{s,a}}$,

$$\pi_{t=0}^{\mathrm{s,a}}(T^{\mathrm{s,a}}) = T^{\mathrm{s,a}} S_{\mathrm{e^-}}^{*} + T^{\mathrm{s,a}} S_{\mathrm{Li^+}}^{*} - T^{\mathrm{s,a}} S_{\mathrm{Li(x)}}^{\mathrm{s,a}} + \sum_{i=1}^{n-1} t_i q_i^{*}. \tag{32}$$

At the stationary state, when diffusion has stopped ($J_i = 0$), the expression simplifies to

$$\pi_{t=\infty}^{\mathrm{s,a}}(T^{\mathrm{s,a}}) = T^{\mathrm{s,a}} S_{\mathrm{e^-}}^{*} + T^{\mathrm{s,a}} S_{\mathrm{Li^+}}^{*} - T^{\mathrm{s,a}} S_{\mathrm{Li(x)}}^{\mathrm{s,a}}. \tag{33}$$

These equations can be used in the model to find the surface temperature. The impact of the Dufour effect is be seen through the Peltier heat. This effect on the Peltier heat has heretofore been unaccounted for in battery modeling. Gunnarshaug *et al.* reported both the initial and stationary state Peltier heat of $LiFePO_4$ and graphite electrodes at 0% state of charge.[24] The difference between the two, equal to the last term in Eq. (10), was significant, motivating us to include the effect here.

We next make the assumption that $\Delta_{\mathrm{a,s}} T/T^{\mathrm{a}}$ and similar terms are small, and that there is equilibrium for adsorption of electrolyte components at the electrode ($\Delta_{\mathrm{s,e}} \mu_{k,T} = 0$). At stationary state, all molar fluxes of neutral components are zero, $J_k^{\mathrm{e,a}} = 0$. We are then left with

$$\frac{\mathrm{d}T^{\mathrm{s,a}}}{\mathrm{d}t} = \frac{1}{\rho^{\mathrm{s,a}} C_p^{\mathrm{s,a}}}\left(-\lambda_{\mathrm{a}}^{\mathrm{s,a}} \Delta_{\mathrm{a,s}} T + \lambda_{\mathrm{e}}^{\mathrm{s,a}} \Delta_{\mathrm{s,e}} T - \frac{\pi_{t=\infty}^{\mathrm{s,a}}}{F} j + r^{\mathrm{s,a}} j^2\right). \tag{34}$$

The first and second terms describe heat conductance to and from the surface, respectively, the third term is the Peltier heat, and the last term stems from the irreversible heat production of the overpotential (the resistance of the electrode to charge transfer). By omitting Dufour effects, we are left with the heat leaking from or into the surfaces from the current collectors, the heat absorbed or produced reversibly, and the heat production due to the overpotential.

The heat effects at the interfaces are in agreement with the local-heat-generation described by Rao and Newman.[10] However, while they gave equations for interface heat sources, they did not describe the temperature variation of the interface. When the left-hand side of the equation above is put equal to zero, the expression is identical to that given by Gu and Wang[17] for the interface energy balance.

We finally give the equivalent equations to Eqs. (32) and (33) for the cathode surface,

$$\pi_{t=\infty}^{\mathrm{s,c}}(T^{\mathrm{s,c}}) = -T^{\mathrm{s,c}} S_{\mathrm{e^-}}^{*} - T^{\mathrm{s,c}} S_{\mathrm{Li^+}}^{*} + T^{\mathrm{s,c}} S_{\mathrm{Li(x)}}^{\mathrm{s,c}}, \tag{35}$$

$$\frac{\mathrm{d}T^{\mathrm{s,c}}}{\mathrm{d}t} = \frac{1}{\rho^{\mathrm{s,c}} C_p^{\mathrm{smc}}}\left(-\lambda_{\mathrm{e}}^{\mathrm{s,c}} \Delta_{\mathrm{e,s}} T + \lambda_{\mathrm{c}}^{\mathrm{s,c}} \Delta_{\mathrm{s,c}} T - \frac{\pi_{t=\infty}^{\mathrm{s,c}}}{F} j + r^{\mathrm{s,c}} j^2\right). \tag{36}$$

IV. METHODS

A. Case studies

The transport properties used in the calculations are presented in Table I (bulk properties) and Table II (surface properties). Properties are estimated for a graphite anode, a lithium iron phosphate (LFP) cathode, and an electrolyte of 1M $LiPF_6$ in EC:DEC (weight ratio 1:1). Here, EC is ethylene carbonate, and DEC is diethyl carbonate.

TABLE I. Transport properties of anode, cathode, and electrolyte materials taken from the literature and used in the base case.

Parameter	Unit	Value
L^a, L^e, L^c	m	7.4×10^{-5}, 1.2×10^{-5}, 6.7×10^{-5}
r^a, r^e, r^c	Ω m	1.4×10^{-5},[34] 6.96×10^{-3},[a] 2.8×10^{-5}[b]
$\lambda^a, \lambda^e, \lambda^c$	W K^{-1} m^{-1}	1.11,[6] 0.31,[6] 0.32[6]
C_p^a, C_p^e, C_p^c	J kg^{-1} K^{-1}	700,[35] 2066,[36] 741[37]
ρ^a, ρ^m, ρ^c	kg m^{-3}	2260,[38] 1000,[38] 2060[37]
$S_{e^-}^{*,a}, S_{Li^+}^{*}, S_{e^-}^{*,c}$	J K^{-1} m^{-3}	5.74,[34] 460,[39] 14.5[40]

[a]Estimated.
[b]Estimated.

The solid electrolyte interface, commonly referred to as the SEI layer within a LIB, was used to estimate the anode surface thickness and properties. For the cathode surface, we assumed the presence of a carbon coating, which is often applied on the LFP particle to increase the performance.[32] For the surface, the thermal conductivity and the excess densities refer to the whole surface area.

The SEI layer on a graphite anode has been shown to partially consist of Li_2CO_3 and LiF.[33] The transport properties for the anode surface were therefore estimated for an equiweight mixture of Li_2CO_3 and LiF, while the transport properties for the cathode surface were taken from literature values for carbon. The resulting input parameter for the surface is presented in Table II.

In all studies, we considered a current density of 30 A m^{-2}. This is a current density that is expected when a fully charged cell is discharged within an hour.

It is not straight forward to find transport coefficients from the literature, which are appropriate for the equations provided by non-equilibrium thermodynamics. Consider Eq. (2) for illustration. The thermal conductivity we are seeking is from this equation, the property measured in the absence of concentration gradients and electric currents (fields). The value we find in the literature must therefore refer to a homogeneous state. Care has been taken to accommodate such conditions, but the set of coefficients in Tables I and II must still be regarded as estimates. The data we need are often lacking, and most seriously so for the surface.

TABLE II. Transport properties for the anode and cathode interfaces taken from the literature and used for the investigation.

Parameter	Unit	Value
$\Delta_{C_6}\phi_{j=0}, \Delta_{LFP}\phi_{j=0}$	V	0.1,[43] 3.45[43]
$j_{0,a}, j_{0,c}$	A m^{-2}	0.8,[30] 1.7[31]
$\delta_{a,s}, \delta_{c,s}$	nm	50,[44] 10
$\lambda^{Na_2CO_3}$,[a] λ^{LiF}	W m^{-1} K^{-1}	0.65,[45] 4.01[46]
$\rho^{Li_2CO_3}, \rho^{LiF}$	kg m^{-3}	2110,[47] 2639[46]
$C_p^{Li_2CO_3}, C_p^{LiF}$	J kg^{-1} K^{-1}	1350,[48] 1562[46]
$\pi_{t=0}^{s,C_6}, \pi_{t=0}^{s,LFP}$	kJmol^{-1}	19,[24] 38[24]
$\pi_{t=\infty}^{s,C_6}, \pi_{t=\infty}^{s,LFP}$	kJ mol^{-1}	104,[24] 122[24]

[a]We assume a similar thermal conductivity of Na_2CO_3 and Li_2CO_3.

The aim of the present work is, however, not so much to provide precise numbers on the profiles but rather to demonstrate the principles of a physical-chemical model, which can be further developed to answer to design issues and reveal a need for more experiments.

1. Base case

A base case was defined to establish a basis for comparison. We used the properties defined in Tables I and II, typical for the battery, and computed the approach of the cell to stationary state in $T(x)$. All coupling effects were included. For the stationary state, we computed local heat fluxes and the entropy production in the system. We also studied the impact of the current density on the temperature profile.

2. Study 1: Surface property variation

The sensitivity of the base case results to variations in the surface properties was examined. Scaling factors k_a and k_c were used to vary conductivities and excess densities [see Eq. (39)].

3. Study 2: Effect of Peltier coefficients

The coupling between heat and charge transfer, the Peltier coefficient, was varied in study 2. We studied the effect on the temperature profile when replaced the local Peltier coefficients by an average value in the whole cell. This mimics the current way that the reversible heat effect is addressed. We computed the results for the cell at the initial state and when all diffusion was stopped (Soret equilibrium).

4. Study 3: Stack profiles

A realistic battery system consists of several unit cells being stacked together, and we studied the behavior of 4–80 such cells. The current collectors were of copper (the anode) and aluminum (the cathode). The current collectors were covered with the active material from both sides and stacked in a repetitive, mirrored manner. Figure 4 presents a sketch of a module of four cells.

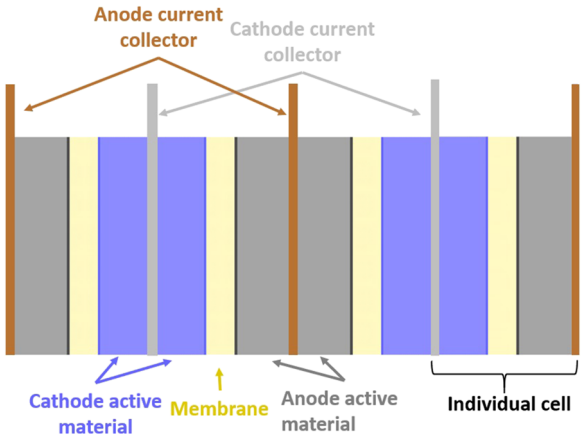

FIG. 4. A LIB stack consisting of four cells. The current collector is coated from both sides with the active material. The anode and cathode are stacked alternating, separated by a separator.

B. Computational procedures

All computations were performed in MATLAB R2019a. All equations are discretized with the finite difference method using an implicit scheme [the Backward Time, Centered Space (*BTCS*) method]. The equations were implemented as presented in the theory with the following assumptions and simplifications:

- When we considered the electrolyte to be in stationary state, we removed the sum over the mass fluxes in the energy balances (34) and (36) and neglected the second to last terms in Eqs. (34) and (36).
- The thermal conductivities of the surface sides were set equal in lack of better information: $\lambda_i^{s,i} = \lambda_i^{o,s} (= \lambda_i^{s})$.
- All transport properties were assumed to be constant. This assumption is fair for shorter times and the temperature range in question.
- The initial temperature of the complete cell was set to the ambient temperature,

$$T(t = 0, x) = T_{amb}. \tag{37}$$

The boundary temperatures were initially fixed to the ambient temperature in order to allow for a thorough examination of internal processes,

$$T(t, x = 0) = T_{amb}\, T(t, x = L) = T_{amb}, \tag{38}$$

where L is the left side boundary and therefore dependent on the case study, the thickness of the unit cell or the cell stack.

- The surface properties were estimated from bulk properties using the method of Kjelstrup and Bedeaux.[12] The bulk main thermal conductivity was divided by the thickness of the surface δ times a dimensionless scaling coefficient k_i. Excess densities, needed in the energy balances, were likewise obtained by multiplying the bulk density with the surface thickness and dimensionless scaling coefficient. A scaling factor equal to one means that surface and bulk properties are equal. A scaling factor larger than one represents an excess surface resistance,

$$\lambda_i^{s} = \frac{\lambda_i}{k_i \delta}\, \rho_i^{s} = k_i \delta \rho_i. \tag{39}$$

By comparing the resistance of the SEI layer[41] to the anode resistance, we obtained a scaling factor for the anode surface of 14. A scaling factor of the cathode surface was estimated so that results on the stack level aligned with both experimental and modeling results.[6,42]

V. RESULTS AND DISCUSSION

A. Base case

The results of the base case are plotted in Figs. 5–8. The results present several aspects of the simultaneous solution of the five sets of equations, one for each cell layer. In Figs. 5–7, we present (1) temperature profiles, with (2) corresponding heat fluxes and (3) entropy production variation through the cell. The current density of the base case was standardly 30 A m^{-2} but was varied in Fig. 8. At the current density 30 A m^{-2}, we calculated a working potential of the cell of 3.3 V.

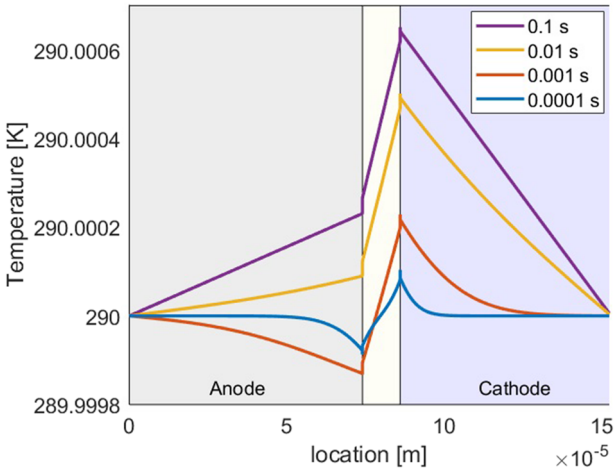

FIG. 5. Temperature profile of the base case after 0.0001 s (blue), 0.001 s (orange), 0.01 s (yellow), and 0.1 s (purple). All results are for 30 A m^{-2}. The profile at 0.1 s corresponds to the stationary state profile. The blue curve at the start documents the Peltier effects: cooling at the anode and heating at the cathode. Multimedia view: https://doi.org/10.1063/5.0038168.1

1. The temperature- and heat flux profile

The time-evolution of the temperature profile to stationary state in about 0.1 s is shown in Fig. 5. Lines of different colors represent different times. Figure 5 is a static representation of the multimedia file, which is linked to the figure. The video shows the continuous transformation of the temperature profile. The cooling at the anode surface and heating at the cathode surface can be well observed during the first fractions of a second (blue curve). We see a heat wave propagating toward the boundaries in the times to follow. Examples are shown for 0.001–0.01 s (red and yellow curves) in the static figure. At the stationary state (0.1 s, purple curve in Fig. 5), we

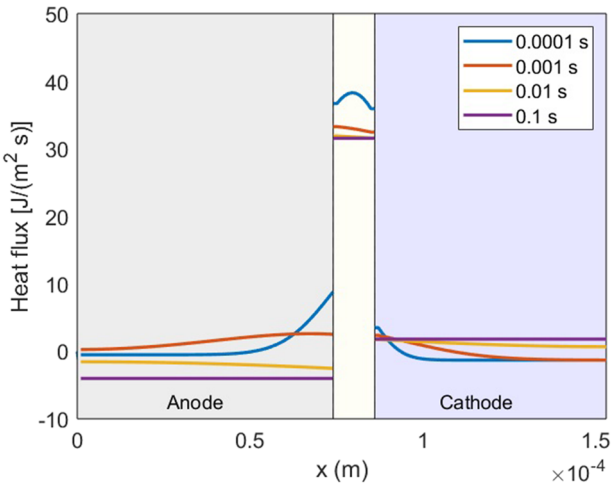

FIG. 6. The heat flux of the base case (corresponds to the temperature profile in Fig. 5) across the cell after 0.0001 s (blue), 0.001 s (orange), 0.01 s (yellow), and 0.1 s (purple) for 30 A m^{-2}.

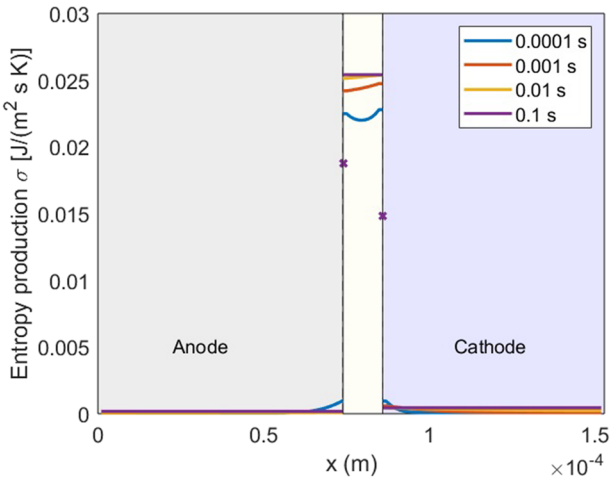

FIG. 7. Profile of the entropy production for the base case (corresponds to the temperature profile in Fig. 5) after 0.0001 s (blue), 0.001 s (orange), 0.01 s (yellow), and 0.1 s (purple) for 30 A m^{-2}. The excess values of the surfaces appear as singularities.

observed characteristic linear profiles within the bulk phases. This behavior follows from fixing the temperature at the boundary to 290 K. The straight lines are also due to constant transport properties. The stationary state temperature profile is maintained after this time.

The temperature is largest at the cathode surface at all times. In the stationary state profile (purple curve), we observed a temperature rise of 0.0006 K. The small values may not appear significant, but we will show for a stack that the temperature can significantly increase if we increase the thickness of the cell and the current density. Moreover, the chosen boundary condition for temperature represents a

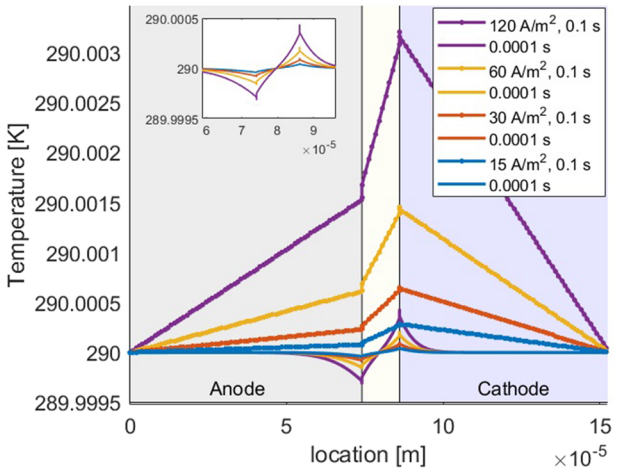

FIG. 8. The temperature profile of the base case as a function of current density. The values are 15 A m^{-2} (blue), 30 A m^{-2} (orange), 60 A m^{-2} (yellow), and 120 A m^{-2} (purple) after 0.0001 s and 0.1 s. Stationary state profiles are given. 0.1 s corresponds to the stationary state profile. The inset enlarges the curves for the shortest times.

perfect cooling of the cell, preventing internal heating. Perfect cooling is, of course, not realistic. The purpose of Figs. 5–8 is therefore not to find the exact values for a single cell, but to better understand the interplay of the various effects, so one can deal with them properly on a later stage.

By inspecting the local effects in the stationary state profile, we further observe temperature jumps across the interfaces. They are ~3 × 10^{-5} K at the both electrode surfaces. The temperature difference across the electrolyte-filled separator in the stationary state is 0.000 35 K, which corresponds to a temperature gradient of 29 K/m. With $S^*_{Li^+}$ = 460 J K^{-1} mol^{-1} from Table II and dT/dx = 29 K/m, the contribution to $d\phi/dx$ over the electrolyte is −0.139 V/m. This temperature gradient presents a local thermal driving force, coupling of heat and mass transfer, as well as heat and charge transfer. The gradients increase with the current density (see below).

The computed temperature profiles have some support from two experimental studies of Heubner *et al.*[49,50] The temperature at a cross section of a single LIB cell was measured using microscopic *in-operando* thermography[50] and thermocouples.[49] A very small temperature difference of the cathode and anode was reported. The experiments were done with different boundary conditions from ours, with an LCO cathode and with larger layer thicknesses. However, they also observed what we see, a temperature decrease in the anode and a temperature increase in the cathode during discharge. Using thermocouples, they measured the temperature difference between the anode and the respective current collector, as well as a temperature difference between the cathode and the respective current collector. A temperature difference between the anode and the cathode of 0.004 K was found during discharge with a current density of 15 A m^{-2}. For comparison, when we applied the same current density and layer thicknesses to our model, as well as the stationary state Peltier heat, we obtained a temperature difference between the anode and the cathode surface of 0.0016 K, in qualitative agreement with Heubner *et al.*

It has to be kept in mind that we consider a simplified system where the properties of two interfacial regions have been contracted. They have been integrated out as Gibbs excess variables. The real system is a porous electrode, with a given porosity, contact areas, and contact lines. It has been common to construct a continuous path through this region.[9,16] In the real system, there are no sharp interfaces but rather many interfaces throughout the electrode bulk materials. When we transfer the results from our coarse-grained system to a more detailed scale, we would expect many small local temperature drops or rises. Our model is less specific when it comes to the electrode interfaces but might well underestimate excess surface resistances. The strength of the model is its direct use of the second law of thermodynamics and therefore the possibility it gives to introduce assumptions in a systematic manner.[23]

The heat flux (Fig. 6) is negative in the anode and positive in the electrolyte and the bulk of the cathode at stationary state. The signs mean that heat is leaving the cell on both sides. We recall that the positive direction of transport is from left to right. The positive heat flux in the electrolyte arises from heat transported with charge, i.e., the Peltier coefficient, since the maximum temperature is located at the cathode. Deviations from constant values are due to varying contributions from Fourier type terms. The large value of the transported entropy of lithium, calculated from Eq. (31) using

values given in Refs. 24, 39, 40, and 51, can be supported by a general observation that large Seebeck coefficients are common with organic electrolytes.[52]

We observed that the absolute value of the heat flux leaving the battery on the anode side was larger than the one on the cathode side. This is again explained by the net heat transported with charge or the large value of the transported entropy of lithium-ions. The difference in the heat flux of the electrolyte and the electrode is mainly due to the Peltier heat for these conditions, which are close to being reversible. The jump in the heat flux is larger in the anode than in the cathode at the stationary state [cf. Eqs. (31) and (32)].

2. The local entropy production

The entropy production will immediately locate the main irreversibilities of the cell.

The local entropy production in the base case is presented in Fig. 7. The surface values are singularities, illustrated by dots. Such singular values are typical for a model that is treating the electrode surfaces as 2D autonomous systems. We observed that the largest entropy production takes place in the electrolyte-filled separator and the two electrode surfaces. This is expected because the resistance is large in the electrolyte-filled membrane. Thermal gradients will, however, also contribute. The entropy production in the surfaces is large due to the overpotentials and the temperature jumps. The entropy production is negligible in the bulk electrodes. This is explained by the significantly larger resistance in the electrolyte compared to the electrodes. It is increasing slightly with time for the bulk phases, and this increase can be ascribed to increasing temperature gradients.

The last figure from the base case, Fig. 8, shows the stationary state temperature profiles as a function of current density. All features shown before are enlarged for larger current densities, as expected. The maximum temperature difference was 0.003 K for a current density of 120 A m^{-2}. The temperature jumps in the anode and cathode surface increased to around 1.2×10^{-4} K, and the temperature gradient in the electrolyte-filled separator for a current density of 120 A m^{-2} was 100 K/m. This results in a contribution to the gradient in electric potential, $d\phi/dx$, over the electrolyte of −0.5 V/m.

B. Study 1: Sensitivity to surface properties

The sensitivity of the temperature profiles to surface properties is reported in Figs. 9 and 10. In these figures, we have presented the initial behavior at 0.0001 s as well as the stationary state profile for various values of the scaling factors. The scaling factors were introduced to measure the deviation of surface properties from bulk ones [cf. Eq. (39)].

It is immediately noticeable that the value of the scaling factor has a large impact not only on the profile shapes but also on the absolute temperatures. The scaling factors, along with the surface heat effects, will define the surface temperature and the heat exchange with the bulk phases.

In Fig. 9, we present the resulting temperature profiles when we increase either k_a or k_c, keeping the other at unity. The inset in Fig. 9 enlarges the initial profiles after 0.0001 s. When k_a increases, while $k_c = 1$ (purple and yellow curve), we observed already at small times that the cooling of the anode surface was more pronounced than

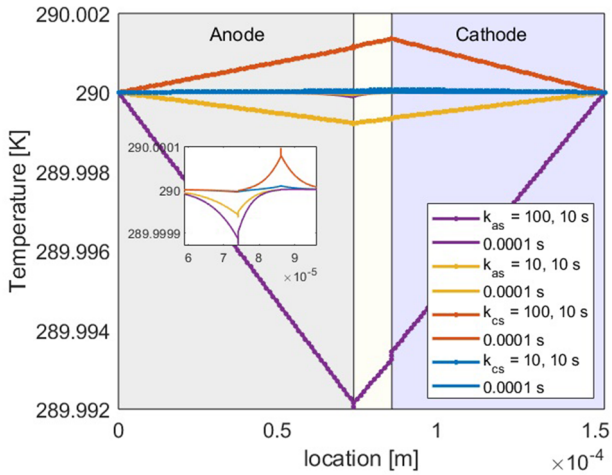

FIG. 9. Temperature profiles for varying scaling factors after 0.0001 and 0.1 s and a current density of 30 A m^{-2}. The profile at 0.1 s corresponds to the stationary state profile. One scaling factor is set to one, while the other is varied. Only the scaling factor that deviates from unity is reported in the legend. The inset enlarges the profiles of the smallest times.

the heating of the cathode surface. The result was an overall cooling of the cell at the stationary state. The effect became more extreme, the larger the difference between the scaling factors for the anode and cathode surfaces were. The situation was reversed when $k_c > k_c$ (orange and blue curve). Again, the heating effect became more pronounced, the larger the difference between the scaling factors were.

With a larger scaling factor, the impact of the interface increased. Recall that the surface thermal conductivity was obtained by dividing the bulk property by the product of the surface thickness and the scaling factor [cf. Eq. (39)]. In Fig. 10, the scaling factors both electrode surfaces varied in parallel, from unity to 10^4. Stationary

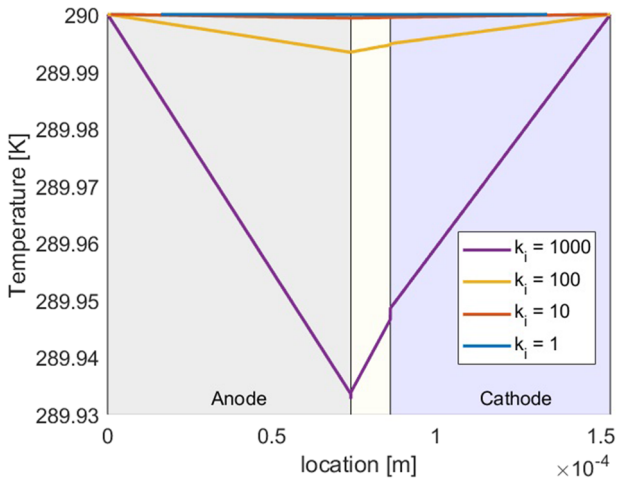

FIG. 10. Stationary state temperature profiles for varying scaling factors. The current density was 30 A m^{-2}. The scaling factor of the anode and the cathode surface is varied in the same manner.

state profiles are presented. The cell temperature was lowered, the lowest temperature being at the anode surface. The effect increased with the scaling factor.

In Eq. (38), we chose a larger surface thickness for the anode surface than for the cathode surface, leaning on SEI measurements. When we estimated surface properties from bulk properties using a surface thickness ($\delta_a > \delta_c$), while the scaling factor remained the same ($k_a = k_c$), we obtained a larger surface resistivity for the anode than for the cathode. Therefore, the behavior of the anode surface dominated the picture when the scaling factors vary in parallel.

An increase in cell temperature has been reported numerous times,[6,53,54] so k_c has to be larger than k_a, as used in Fig. 9. As we used a larger surface thickness for the anode than for the cathode, a larger k_c than k_a will to some extent compensate for the difference in surface thicknesses.

We have chosen to model the SEI layer on the anode as an anode surface and used an anode thickness of 50 nm. This is large for a molecular surface but small for the SEI layer. For the SEI layer on carbon coated graphite, a thickness up to 150 nm has been reported. For uncoated graphite spheres, a SEI layer thickness was reported to be from 450 to 980 nm.[55] The surface is defined as the location where the reaction happens and therefore considered to be thin. These results suggest treating also the SEI layer as a bulk phase in future work and relocating the surface.

C. Study 2: Peltier effects

This case was designed to investigate contributions from the Peltier effect on the temperature profile in the homogeneous phases and on the temperature jumps at the electrodes. In the following, we use the acronym RHE for reversible heat effects. We compare temperature profiles for average and local RHE [cf. Eq. (33)] in Fig. 11 both after 0.0001 and 0.1 s. The initial Peltier heat estimated from the Seebeck coefficient in a homogeneous solution was denoted $\pi^s_{t=0}$, while the stationary-state Peltier heat estimated from the Seebeck coefficient at Soret equilibrium is denoted $\pi^s_{t=\infty}$. We are reaching the stationary state temperature profile after 0.1 s. The results for $\pi^s_{t=\infty}$ are the same as the base case (Fig. 5).

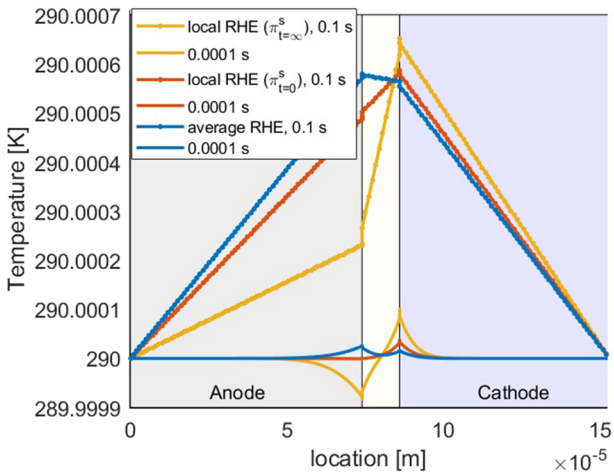

FIG. 11. Temperature profile for average reversible heat effects (RHE) (blue) and in the presence of local initial RHE $\pi^s_{t=0}$ (orange) and local stationary-state RHE $\pi^s_{t=\infty}$ (yellow) at a current density of 30 A m^{-2}.

For the average RHE scenario (blue curve), we observed heating at both electrode surfaces. The heating was now solely due to reaction overpotentials and due to the overall entropy change of the battery, which was ascribed equally to both surfaces. This particular model mimics the thermal modeling, which is common in the literature.[6,56–58]

For the local RHE, we observed always a cooling effect at the anode surface during discharge. The cooling was stronger at $\pi^s_{t=\infty}$ (yellow curve) compared to $\pi^s_{t=0}$ (orange curve). For the averaged RHE, we observed a more evenly distributed temperature profile after 0.1 s and an simultaneous underestimation of the cathode surface temperature and overestimation of the anode surface temperature. The Peltier heat at infinite time measurement, $\pi^s_{t=\infty}$, takes also into account the Dufour heat.

We observed a large variation in the temperature gradient in the electrolyte-filled separator after 0.1 s. It was only around 1 K/m for the average RHE, 7 K/m for the local RHE with $\pi^s_{t=0}$, and was as large as 29 K/m for the local RHE with $\pi^s_{t=\infty}$.

Local cooling or heating by a few degrees has been observed in an aluminum electrolysis cell.[59] A temperature reduction was observed at the anode at an average electrolyte temperature of 960 °C. The effect was explained by a large Seebeck coefficient, 3.6 mV/K. A LFP-electrode has for comparison a Seebeck coefficient of 4.3 mV/K, so we may speculate that a similar cooling can occur here. With the fixed temperature boundary conditions used in the present model, we do not expect large cooling effects, however. The boundary conditions, simulation time, and the other transport properties will not favor this. The purpose of this work is to document a new physical-chemical model, compare it to presently used models, and demonstrate their difference.

D. Study 3: Stacking

A commercial LIB is a stack containing several single cells. We present the initial and stationary state temperature profile of a double cell (Fig. 12), two double cells (Fig. 13), and ten double cells (Fig. 14). In all simulations, we used the parameters of the base case. In addition, we compared the stationary state temperature profile of ten double cells for local and average RHE (Fig. 15).

Figure 12 shows the temperature profile of a double cell consisting of two single cells stacked in a repetitive, mirrored manner. Figure 13 presents the temperature profile for two double cells—four cells in total. The sets of vertical straight lines mark the anode and cathode surfaces. The horizontal lines in the center, most pronounced in the temperature profile after 100 s (purple curve) (first at 0.15 mm), indicate positions of current collectors. Because the thermal conductivity of the current collector material is significantly larger than that of the electrodes and the electrolyte, there is nearly no temperature gradient in the current collectors. Figure 14 presents the temperature profile for a stack of ten double cells, 20 cells in total. The inset in Fig. 14 enlarges parts of the initial temperature profiles after 0.0001 s (blue curve) and 0.01 s (orange curve). It illustrates the Peltier effect in the single cells of a stack: we observe the cooling at the anode surface and the heating at the cathode surface.

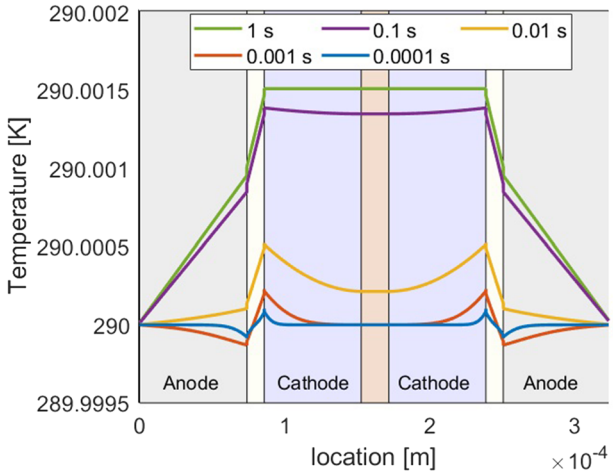

FIG. 12. Temperature profile for a double cell consisting of the anode–separator–cathode–cathode current collector–cathode–separator–anode. Profiles presented after 0.0001 s (blue), 0.001 s (orange), 0.01 s (yellow), 0.1 s (purple), and 1 s (green) and a current density of 30 A m^{-2}. A stationary state is reached after 1 s.

We see that the temperature increase with time is amplified in a cell stack compared to a single cell (Fig. 5), the largest temperature being observed in a cathode in the middle of the cell. In all stack simulations, we observed an oscillating temperature profile at initial times (0.0001 s), the lowest temperatures being in the anodes, as pictured in Fig. 13.

With a small cell stack of only 2–4 cells, we reached the stationary state temperature profile after 1 s, while a cell stack of 20 cells needed 20 s to reach the stationary state. Therefore, the temperature profile after 100 s (purple curve) overlaps with the profile after 1 s (yellow curve) in Figs. 12 and 13. The reason for a rapid approach to stationary state is the chosen fixed thermal boundary conditions and the chosen physical parameters. As we only simulate for very short time periods, it is fair to neglect a change in the state of charge.

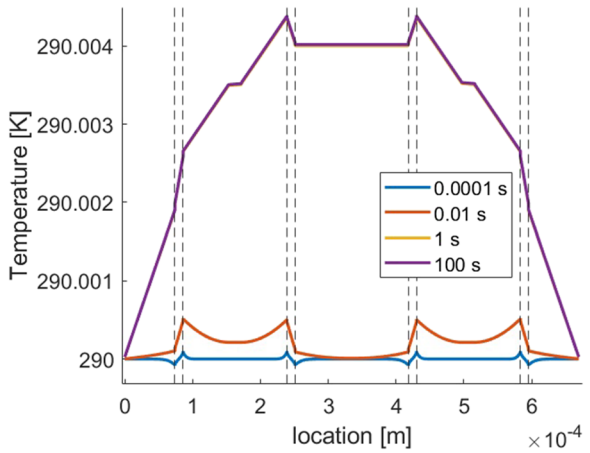

FIG. 13. Temperature profile for a stack of four cells after 0.0001 s (blue), 0.01 s (orange), 1 s (yellow), and 100 s (purple) and a current density of 30 A m^{-2}. The dashed lines mark the surfaces.

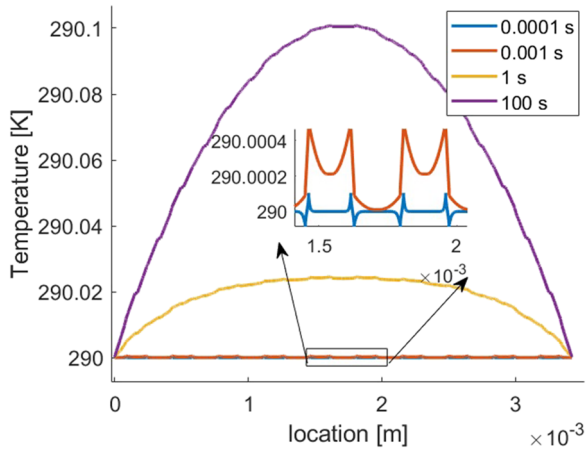

FIG. 14. Temperature profile of a stack of 20 cells after 0.0001 s (blue), 0.01 s (orange), 1 s (yellow), and 100 s (purple) and a current density of 30 A m^{-2}.

As expected, the temperature profile across a cell is a clear function of battery thickness. While it is only around 0.0007 K for a single cell, it reaches around 0.1 K for a stack of 20 cells. This might appear to be small, but will increase significantly, when the current density (cf. also Fig. 8) and the thickness of the stack are increased. As an example, by increasing the current density from 30 to 120 A m^{-2}, we increased the maximum temperature from 0.0007 to 0.003 K (Fig. 8). For a stack of 20 cells, we computed a maximum temperature rise of 0.1 K with a current density of 30 A m^{-2}. In a stack of 40 cells (battery thickness ~7 mm) and a current density of 60 A m^{-2}, the temperature rise was 0.9 K. This is well within the range of what has been reported in the literature, measured[42] and modeled.[6] Figure 16 shows how large the temperature rise within one battery can become when we consider the case of a thick battery stack of 80 cells and a high current density of 120 A m^{-2}. The maximum battery temperature rise is 8.5 K higher than the surface temperature in the presence

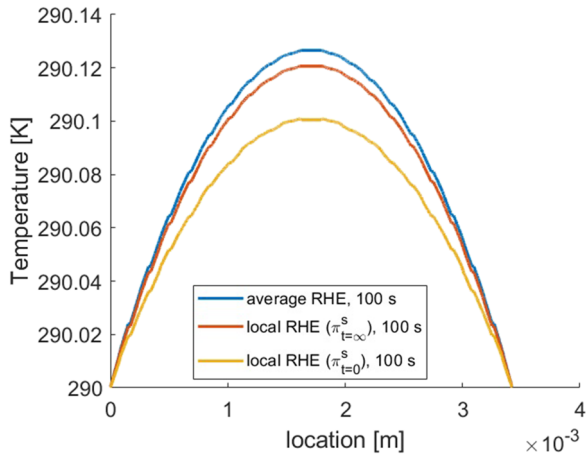

FIG. 15. Temperature profile of a stack of 20 cells including average RHE (blue), initial local RHE $\pi^s_{t=0}$ (orange), and stationary-state local RHE $\pi^s_{t=\infty}$ (yellow) at a current density of 30 A m^{-2}.

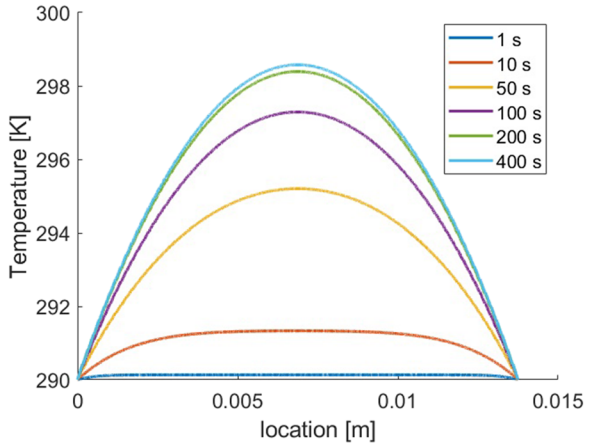

FIG. 16. Temperature profile of a stack of 80 cells after 1, 10, 50, 100, 200, 300, and 400 s and a current density of 120 A m^{-2}.

of external cooling. The initial temperature profiles after only a short discharge [1 s (blue curve) and 10 s (orange curve)] are still quite flat. Large variations can only be found between the cells adjacent to the battery surface. After around a minute of discharge (orange curve), the difference between the cells starts to vary, the hottest cell in the stack being in the center. A large difference between cell temperatures within one battery has been shown to have a severe impact on the internal resistances, current distribution, and degradation of LIB.[60]

Figure 15 shows how the stack temperature profile is affected when reversible heat effects are modeled as local (orange and yellow curve) or averaged out (blue curve). The results from a unit cell (Fig. 11) are now amplified. The temperature in the stack center is highest when average RHE is used in the model, closely followed by results with the initial Peltier heats, while the temperature increase at the cathode surface is reduced by 20% when the stationary state Peltier heats are implemented. We recall that the difference between the two last values is given by the Dufour effect [see Eqs. (32) and (33)]. We see that the Dufour effect can have an important contribution to the surface temperature.

Many authors claim that reversible heat effects are only significant at the low discharge rate. Theory predicts that reversible heat effects are proportional to the electric current, while the irreversible effects are non-linear in the current density. In this sense, the irreversible terms will always dominate at a certain high current density. This is not to say that the reversible terms are not significant; they may, for instance, help cool an otherwise too hot electrode surface.

E. Comments on the theoretical description

We have seen above and in the supplementary material that the full description in terms of non-equilibrium thermodynamics soon becomes rather complex. It is, however, comforting to see how simpler expressions, now common in the literature, are contained in the complex formulation, as they must be. We have given the full expressions with the hope that we, with access to more experimental results, will be able to solve the equation set also for conditions that now have been neglected because of lack of data and find more precise values for cell properties. Clearly, there is a need to measure more properties, especially interface properties.

One purpose of the theoretical elaboration has been to elucidate theoretical expressions now used in battery research. This relates, in particular, to the common expression for heat generation,[9,17,61,62]

$$Q = I\left(\Delta_{tot}\phi - \Delta_{tot}\phi_{j=0} + T\frac{d(\Delta_{tot}\phi_{j=0})}{dT} + M\bar{C}_p\frac{dT}{dt}\right), \qquad (40)$$

where A is the cross-sectional area, $I = Aj$ the electric current, $Q = qA$ is the total heat produced, M is the mass, and $\bar{C}_p$ is the mean specific heat capacity of the cell. The *emf*, $\Delta_{tot}\phi_{j=0}$, usually refers to the average state of charge of the electrodes.[15] The two first terms on the right-hand side contain the Joule heat and heat effects due to the overpotential. The second term is the reversible heat effect of the *whole* battery, and the last term is due to heat exchange with the surroundings.

The supplementary material gives a similar expression for the total cell with the same irreversible and reversible heat effects, *but only under the condition of constant temperature and uniform electrolyte*. In the expression above, the local heating and cooling effects have been combined. In other words, local effects have been averaged out, and the thermal model has become less precise. In particular, the expression does not include Dufour and Peltier effects in the heat fluxes. Therefore, it is bound to give incorrect predictions of the heat fluxes at the boundaries [see Eqs. (77) and (92) of the supplementary material].

When it comes to interfaces, also the expression for the time rate of change of the interface temperature differs from expressions given in the literature.[17,63] We allow a separate temperature of the surface, meaning that the surface temperature can vary according to surface properties, in particular, according to surface excess properties. Gu and Wang[17] instead provided equations for the interface that do not allow for storage of heat and/or components at the surface. In short, they do not include the term dT^s/dt (see also Ref. 18). The results in Figs. 9 and 10 show that the surface temperature, together with the scaling factor, defines the temperature profile of the cell. Latz and Zausch[63] presented a continuous rather than discrete surface treatment. They considered the surface volume to be equal to that of the double layer and always in a stationary state mode of operation.

In contrast, the results presented above introduce the surface as a separate thermodynamic system with its own temperature and other properties and present computed results for the surface properties as singularities in the profile (see, e.g., Fig. 7).

In this analysis of the LIB using non-equilibrium thermodynamics, our aim has been to bring forward a better understanding of the interplay of various transport processes or how they are coupled. The observed temperature variations in a single cell may seem negligibly small. However, these are not difficult to enlarge using larger current densities, larger scaling factors, different boundary conditions, or more complex electrolytes. To do so will, however, not make the theoretical model more convincing. Once we understand the interactions in question, more realistic models may be used, however. It is then very interesting to see that a model providing so small effects for one cell can, when combined to larger modules, provide realistic thermal signatures.

F. Implications for further experiments

The aim of the present work is to present a physical-chemical model that can be further developed to answer questions related to design issues and reveal needs for more experiments. The temperature profiles presented here should be regarded in this context. Several of them are not meant to provide insight into real battery operation since we do not use simulation times beyond some seconds. The results make, however, clear that the Peltier effect overrules the picture created by a single Joule effect in the start of the simulation and when the electric current density is small. The total picture is a synthesis of all effects, and the total picture will change significantly if some parts are missing.

It is not simple to distinguish experimentally between single contributions to an overall heat effect. However, attempts have been made to decompose data from electrochemical cells using a second degree polynomial in j (see Refs. 59 and 64). Such a function for the temperature can be understood from the equations used. The possibility to measure Seebeck coefficients is very important, as we can deduce its reciprocal effect, the Peltier heat, which is difficult to measure. Seebeck coefficients will also provide insight into another potentially large effect, the Dufour effect, which can be inferred from the data on Soret equilibrium. Measurements on these properties using battery electrolytes are presently lacking.

We have only been able to include the Dufour effect in a special case: at the stationary state (Soret equilibrium). In this situation, the organic carbonate mixture can be treated as one component.[63] The time-variation of the Peltier heat measured by Gunnarshaug[39] indicates, however, that the organic carbonates may separate in a thermal field and may therefore contribute to the time-evolution. In order to obtain reliable data for the Peltier and Dufour coefficients, we conclude that it is central to measure Seebeck coefficients not only for homogeneous electrolytes but also at the stationary state. To reach this state by diffusion may take more than one day.[24,51] This long time may explain why the change has been overlooked by several investigators.[65–67]

Among other lines of research to be further investigated is the impact of the state of charge on the model.[68] Here, we considered a completely charged cell and a simulation time so small that it does not change the state of charge noticeably. This must be relaxed in the future. Most important is to also change the boundary condition of perfect cooling. To include, a rate-limiting step for heat transfer to the ambient will drastically change the profiles inside the battery.[68]

VI. CONCLUSION

We have documented for the first time a physical-chemical model for LIBs that enables us to describe the full interplay of reversible and irreversible heat effects including the particular role of the surface. We have seen that

- Peltier and Dufour effects need to be included to understand and be able to deal precisely with thermal effects in LIBs.
- The surface excess resistances (the scaling factors), along with the surface heat effects, define the surface temperature and the heat exchange with the bulk phases.
- The interface resistances can lead to local temperature gradients. Values around 29 K/m in the electrolyte-filled separator are typical for moderate current densities (30 A m^{-2}) and a basis set of transport properties.
- The same set of equations that give apparently small or negligible effects in a single cell can under special circumstances combine to a situation that is detrimental, in particular, for a cell stack. In a module of 80 cells, we obtained an internal stationary state temperature rise above 8.5 K after 400 s under the assumption of perfect cooling.

These results are pointing to the need for more accurate knowledge on all transport properties, in particular, of the surfaces, but also of the bulk electrolyte. The method presented was recently used to describe similar heat effects in the polymer electrolyte fuel cells.[23] It is a general method, and we hope to have shown that other electrochemical systems also may benefit from similar analysis.

SUPPLEMENTARY MATERIAL

The supplementary material provides a full derivation of the model applied.

AUTHORS' CONTRIBUTIONS

L. Spitthoff and A. F. Gunnarshaug contributed equally to this work and should be considered as co-first authors.

ACKNOWLEDGMENTS

The authors are grateful to Marco Sauermoser for help with the choice of software and Michael Rauter for initial help with the parameterization. A.F.G., S.K., and D.B. acknowledge the Norwegian Research Council for their Center of Excellence funding scheme for Project No. 262644 PoreLab. L.S. and O.B. acknowledge the financial support from the Research Council of Norway, via the research project BattMarine (Project No. 281005), and from the Norwegian University of Science and Technology (NTNU), via the strategic research program ENERSENSE (Project No. 68024013).

DATA AVAILABILITY

The data that support the findings of this study are available within the article and its supplementary material.

REFERENCES

[1]R. Marom, S. F. Amalraj, N. Leifer, D. Jacob, and D. Aurbach, "A review of advanced and practical lithium battery materials," J. Mater. Chem. **21**, 9938 (2011).
[2]J. B. Goodenough and Y. Kim, "Challenges for rechargeable Li batteries," Chem. Mater. **22**, 587–603 (2010).
[3]H. Liu, Z. Wei, W. He, and J. Zhao, "Thermal issues about Li-ion batteries and recent progress in battery thermal management systems: A review," Energy Convers. Manage. **150**, 304–330 (2017).
[4]E. V. Thomas, H. L. Case, D. H. Doughty, R. G. Jungst, G. Nagasubramanian, and E. P. Roth, "Accelerated power degradation of Li-ion cells," J. Power Sources **124**, 254–260 (2003).
[5]J. Fan and S. Tan, "Studies on charging lithium-ion cells at low temperatures," J. Electrochem. Soc. **153**, A1081 (2006).
[6]F. Richter, S. Kjelstrup, P. J. S. Vie, and O. S. Burheim, "Thermal conductivity and internal temperature profiles of Li-ion secondary batteries," J. Power Sources **359**, 592–600 (2017).

[7]T. Waldmann, M. Wilka, M. Kasper, M. Fleischhammer, and M. Wohlfahrt-Mehrens, "Temperature dependent ageing mechanisms in lithium-ion batteries—a post-mortem study," J. Power Sources **262**, 129–135 (2014).
[8]D. H. Doughty and E. P. Roth, "A general discussion of Li ion battery safety," Electrochem. Soc. Interface **21**, 37 (2012).
[9]D. Bernardi, E. Pawlikowski, and J. Newman, "A general energy balance for battery systems," J. Electrochem. Soc. **132**, 5–12 (1985).
[10]L. Rao and J. Newman, "Heat-generation rate and general energy balance for insertion battery systems," J. Electrochem. Soc. **144**, 2697 (1997).
[11]K. S. Førland, T. Førland, and S. K. Ratkje, *Irreversible Thermodynamics: Theory and Applications* (John Wiley & Sons, Inc., 1988).
[12]S. Kjelstrup and D. Bedeaux, *Non-Equilibrium Thermodynamics of Heterogeneous Systems* (World Scientific, 2020), Vol. 20.
[13]M. Doyle, T. F. Fuller, and J. Newman, "Modeling of galvanostatic charge and discharge of the lithium/polymer/insertion cell," J. Electrochem. Soc. **140**, 1526–1533 (1993).
[14]C. R. Pals and J. Newman, "Thermal modeling of the lithium/polymer battery: I. Discharge behavior of a single cell," J. Electrochem. Soc. **142**, 3274–3281 (1995).
[15]K. E. Thomas and J. Newman, "Heats of mixing and of entropy in porous insertion electrodes," in *papers presented at the 11th International Meeting on Lithium Batteries* [J. Power Sources **119-121**, 844–849 (2003)].
[16]J. Newman, K. E. Thomas, H. Hafezi, and D. R. Wheeler, "Modeling of lithium-ion batteries," in *paper presented at the 11th International Meeting on Lithium Batteries* [J. Power Sources **119-121**, 838–843 (2003)].
[17]W. B. Gu and C. Y. Wang, "Thermal-electrochemical modeling of battery systems," J. Electrochem. Soc. **147**, 2910 (2000).
[18]J. Newman, "Thermoelectric effects in electrochemical systems," Ind. Eng. Chem. Res. **34**, 3208–3216 (1995).
[19]K. E. Thomas and J. Newman, "Thermal modeling of porous insertion electrodes," J. Electrochem. Soc. **150**, A176 (2003).
[20]P. Verma, P. Maire, and P. Novák, "A review of the features and analyses of the solid electrolyte interphase in Li-ion batteries," Electrochim. Acta **55**, 6332–6341 (2010).
[21]S. J. An, J. Li, C. Daniel, D. Mohanty, S. Nagpure, and D. L. Wood III, "The state of understanding of the lithium-ion-battery graphite solid electrolyte interphase (SEI) and its relationship to formation cycling," Carbon **105**, 52–76 (2016).
[22]D. Bedeaux, A. M. Albano, and P. Mazur, "Boundary conditions and non-equilibrium thermodynamics," Physica A **82**, 438–462 (1976).
[23]M. Sauermoser, S. Kjelstrup, and B. G. Pollet, "The impact of Peltier and Dufour coefficients on heat fluxes and temperature profiles in the polymer electrolyte fuel cells," J. Electrochem. Soc. **167**, 144503 (2020).
[24]A. F. Gunnarshaug, S. Kjelstrup, D. Bedeaux, F. Richter, and O. S. Burheim, "The reversible heat effects at lithium iron phosphate-and graphite electrodes," Electrochim. Acta **337**, 135567 (2020).
[25]A. F. Gunnarshaug, S. Kjelstrup, and D. Bedeaux, "The heat of transfer and the Peltier coefficient of electrolytes," Chem. Phys. Lett.: X **5**, 100040 (2020).
[26]A. K. Padhi, K. S. Nanjundaswamy, and J. B. Goodenough, "Phospho-olivines as positive-electrode materials for rechargeable lithium batteries," J. Electrochem. Soc. **144**, 1188–1194 (1997).
[27]K. Jalkanen, T. Aho, and K. Vuorilehto, "Entropy change effects on the thermal behavior of a $LiFePO_4$/graphite lithium-ion cell at different states of charge," J. Power Sources **243**, 354–360 (2013).
[28]V. Srinivasan and J. Newman, "Discharge model for the lithium iron-phosphate electrode," J. Electrochem. Soc. **151**, A1517 (2004).
[29]F. Baronti, W. Zamboni, R. Roncella, R. Saletti, and G. Spagnuolo, "Open-circuit voltage measurement of lithium-iron-phosphate batteries," in *2015 IEEE International Instrumentation and Measurement Technology Conference (I2MTC) Proceedings* (IEEE, 2015), pp. 1711–1716.
[30]H. Ge, T. Aoki, N. Ikeda, S. Suga, T. Isobe, Z. Li, Y. Tabuchi, and J. Zhang, "Investigating lithium plating in lithium-ion batteries at low temperatures using electrochemical model with NMR assisted parameterization," J. Electrochem. Soc. **164**, A1050–A1060 (2017).
[31]C. Heubner, M. Schneider, and A. Michaelis, "Investigation of charge transfer kinetics of Li-intercalation in $LiFePO_4$," J. Power Sources **288**, 115–120 (2015).
[32]Z.-X. Chi, W. Zhang, F.-Q. Cheng, J.-T. Chen, A.-M. Cao, and L.-J. Wan, "Optimizing the carbon coating on $LiFePO_4$ for improved battery performance," RSC Adv. **4**, 7795–7798 (2014).
[33]A. M. Andersson and K. Edström, "Chemical composition and morphology of the elevated temperature SEI on graphite," J. Electrochem. Soc. **148**, A1100 (2001).
[34]E. M. Hansen, E. Egner, and S. Kjelstrup, "Peltier effects in electrode carbon," Metall. Mater. Trans. B **29**, 69–76 (1998).
[35]V. Shen, D. Siderius, W. Krekelberg, and H. Hatch, NIST Standard Reference Simulation Website, NIST Standard Reference Database Number 173, National Institute of Standards and Technology; retrieved 26 October 2020.
[36]S. C. Chen, C. C. Wan, and Y. Y. Wang, "Thermal analysis of lithium-ion batteries," J. Power Sources **140**, 111–124 (2005).
[37]J. Nanda, S. K. Martha, W. D. Porter, H. Wang, N. J. Dudney, M. D. Radin, and D. J. Siegel, "Thermophysical properties of $LiFePO_4$ cathodes with carbonized pitch coatings and organic binders: Experiments and first-principles modeling," J. Power Sources **251**, 8–13 (2014).
[38]V. Vishwakarma, C. Waghela, Z. Wei, R. Prasher, S. C. Nagpure, J. Li, F. Liu, C. Daniel, and A. Jain, "Heat transfer enhancement in a lithium-ion cell through improved material-level thermal transport," J. Power Sources **300**, 123–131 (2015).
[39]A. F. Gunnarshaug, "Thermoelectric properties of non-aqueous electrochemical cells-local reversible heat effects relevant for lithium ion batteries," M.S. thesis, NTNU, 2018.
[40]J. Molenda, A. Kulka, A. Milewska, W. Zając, and K. Świerczek, "Structural, transport and electrochemical properties of $LiFePO_4$ substituted in lithium and iron sublattices (Al, Zr, W, Mn, Co and Ni)," Materials **6**, 1656–1687 (2013).
[41]T. Momma, M. Matsunaga, D. Mukoyama, and T. Osaka, "AC impedance analysis of lithium ion battery under temperature control," J. Power Sources **216**, 304–307 (2012).
[42]Z. Li, J. Zhang, B. Wu, J. Huang, Z. Nie, Y. Sun, F. An, and N. Wu, "Examining temporal and spatial variations of internal temperature in large-format laminated battery with embedded thermocouples," J. Power Sources **241**, 536–553 (2013).
[43]K. C. Kam and M. M. Doeff, "Electrode materials for lithium ion batteries," Mater. Matters **7**, 56 (2012).
[44]A. Wang, S. Kadam, H. Li, S. Shi, and Y. Qi, "Review on modeling of the anode solid electrolyte interphase (SEI) for lithium-ion batteries," npj Comput. Mater. **4**, 15 (2018).
[45]G. Pan, J. Ding, W. Wang, and X. Wei, "Molecular simulations of the thermal and transport properties of molten alkali carbonates," Energy Procedia **105**, 4377–4382 (2017).
[46]See https://www.sigmaaldrich.com/catalog/product/aldrich/449903?lang=en&region=NO for Lithium fluoride, Sigma-Aldrich, data sheet; accessed 17 November 2020.
[47]D. Lide, *Handbook of Chemistry and Physics*, 86th ed. (CRC, 2005).
[48]L. Kourkova and G. Sadovska, "Heat capacity, enthalpy and entropy of Li_2CO_3 at 303.15–563.15 K," Thermochim. Acta **452**, 80–81 (2007).
[49]C. Heubner, M. Schneider, C. Lämmel, U. Langklotz, and A. Michaelis, "*In-operando* temperature measurement across the interfaces of a lithium-ion battery cell," Electrochim. Acta **113**, 730–734 (2013).
[50]C. Heubner, C. Lämmel, N. Junker, M. Schneider, and A. Michaelis, "Microscopic in-operando thermography at the cross section of a single lithium ion battery stack," Electrochem. Commun. **48**, 130–133 (2014).
[51]F. Richter, A. Gunnarshaug, O. S. Burheim, P. J. S. Vie, and S. Kjelstrup, "Single electrode entropy change for $LiCoO_2$ electrodes," ECS Trans. **80**, 219–238 (2017).
[52]M. Bonetti, S. Nakamae, M. Roger, and P. Guenoun, "Huge Seebeck coefficients in nonaqueous electrolytes," J. Chem. Phys. **134**, 114513 (2011).
[53]S. Novais, M. Nascimento, L. Grande, M. F. Domingues, P. Antunes, N. Alberto, C. Leitão, R. Oliveira, S. Koch, G. T. Kim *et al.*, "Internal and external temperature monitoring of a Li-ion battery with fiber Bragg grating sensors," Sensors **16**, 1394 (2016).
[54]T. M. Bandhauer, S. Garimella, and T. F. Fuller, "Temperature-dependent electrochemical heat generation in a commercial lithium-ion battery," J. Power Sources **247**, 618–628 (2014).

[55]S. Goriparti, E. Miele, F. de Angelis, E. Di Fabrizio, R. Proietti Zaccaria, and C. Capiglia, "Review on recent progress of nanostructured anode materials for Li-ion batteries," J. Power Sources **257**, 421–443 (2014).
[56]Z. An, L. Jia, L. Wei, C. Dang, and Q. Peng, "Investigation on lithium-ion battery electrochemical and thermal characteristic based on electrochemical-thermal coupled model," Appl. Therm. Eng. **137**, 792–807 (2018).
[57]N. Damay, C. Forgez, M.-P. Bichat, and G. Friedrich, "Thermal modeling of large prismatic $LiFePO_4$/graphite battery. Coupled thermal and heat generation models for characterization and simulation," J. Power Sources **283**, 37–45 (2015).
[58]S. Du, M. Jia, Y. Cheng, Y. Tang, H. Zhang, L. Ai, K. Zhang, and Y. Lai, "Study on the thermal behaviors of power lithium iron phosphate (LFP) aluminum-laminated battery with different tab configurations," Int. J. Therm. Sci. **89**, 327–336 (2015).
[59]S. Kjelstrup, E. Olsen, and J. Qian, "The Peltier heating of aluminium, oxygen and carbon–carbon dioxide electrodes in an electrolyte of sodium and aluminium fluorides saturated with alumina," Electrochim. Acta **46**, 1141–1150 (2001).
[60]G. M. Cavalheiro, T. Iriyama, G. J. Nelson, S. Huang, and G. Zhang, "Effects of nonuniform temperature distribution on degradation of lithium-ion batteries," J. Electrochem. Energy Convers. Storage **17**, 021101 (2020).
[61]U. S. Kim, J. Yi, C. B. Shin, T. Han, and S. Park, "Modelling the thermal behaviour of a lithium-ion battery during charge," J. Power Sources **196**, 5115–5121 (2011).
[62]K. Kumaresan, G. Sikha, and R. E. White, "Thermal model for a Li-ion cell," J. Electrochem. Soc. **155**, A164 (2008).
[63]A. Latz and J. Zausch, "Thermodynamic consistent transport theory of Li-ion batteries," J. Power Sources **196**, 3296–3302 (2011).
[64]P. J. S. Vie and S. Kjelstrup, "Thermal conductivities from temperature profiles in the polymer electrolyte fuel cell," Electrochim. Acta **49**, 1069–1077 (2004).
[65]N. S. Hudak and G. G. Amatucci, "Energy harvesting and storage with lithium-ion thermogalvanic cells," J. Electrochem. Soc. **158**, A572–A579 (2011).
[66]Q. Huang, M. Yan, and Z. Jiang, "Thermal study on single electrodes in lithium-ion battery," J. Power Sources **156**, 541–546 (2006).
[67]J. J. Black, J. B. Harper, and L. Aldous, "Temperature effect upon the thermoelectrochemical potential generated between lithium metal and lithium ion intercalation electrodes in symmetric and asymmetric battery arrangements," Electrochem. Commun. **86**, 153–156 (2018).
[68]V. V. Viswanathan, D. Choi, D. Wang, W. Xu, S. Towne, R. E. Williford, J.-G. Zhang, J. Liu, and Z. Yang, "Effect of entropy change of lithium intercalation in cathodes and anodes on Li-ion battery thermal management," J. Power Sources **195**, 3720–3729 (2010).